Available online at www.sciencedirect.com

ScienceDirect

Geochimica et Cosmochimica Acta 199 (2017) 1–12

Geochimica et Cosmochimica Acta

www.elsevier.com/locate/gca

# Metal–silicate partitioning of U: Implications for the heat budget of the core and evidence for reduced U in the mantle

Bethany A. Chidester [a,*], Zia Rahman [b,c], Kevin Righter [c], Andrew J. Campbell [a]

[a] Department of the Geophysical Sciences, University of Chicago, Chicago, IL 60637, United States
[b] Jacobs, NASA Johnson Space Center, Houston, TX 77058, United States
[c] NASA Johnson Space Center, Houston, TX 77058, United States

Received 5 August 2016; accepted in revised form 20 November 2016; available online 1 December 2016

**Abstract**

Earth's core might require an internal heat source, such as radioactive decay, to explain the presence of the magnetic field through geologic time. To investigate whether U would be an important heat source in the core, we performed metal–silicate partitioning experiments of U at *P–T* (up to 67 GPa and 5400 K) conditions more relevant to a magma ocean scenario than has previously been reported. This study finds the partitioning of U to be strongly dependent on $fO_2$, temperature, the S content of the metal and the $SiO_2$ content of the silicate during core-mantle differentiation. Differentiation at mean conditions of 42–58 GPa and 3900–4200 K would put 1.4–3.5 ppb U (2–8 wt% S) in the core, amounting to a maximum of 1.4 (+1/−0.7) TW of heat 4.5 billion years ago. This is likely not enough heat to mitigate early widespread mantle melting. It was also found that U likely exists in the 2+ oxidation state in silicate melts in the deep Earth, a state which has not been previously observed in nature.


*Keywords:* Uranium; Radiogenic heat; Core energy budget; Magma ocean

## 1. INTRODUCTION

The Earth is a heat engine, driven by secular cooling, radioactive decay and the segregation and solidification of materials into distinct layers (Verhoogen, 1980). Of these heat sources, the decay of the long-lived radioactive isotopes $^{235,238}U$, $^{232}Th$ and, $^{40}K$ account for up to half of the total heat flux at the surface of the planet (Lay et al., 2008). The distribution of these elements in the deep Earth may have profound implications for the heat budget of the core, including the age of the inner core and the source of the geodynamo that has driven the Earth's magnetic field through geologic time, as well as the thermal evolution of the mantle (Labrosse et al., 2001). Whether these radioactive elements are an important heat source in the core itself has been uncertain. Based on the strongly lithophilic nature of these elements at ambient conditions, it has been considered unlikely that they would partition into the metallic phase as the core segregated (McDonough and Sun, 1995). However, it is difficult to reconcile the presence of a geomagnetic field prior to the initiation of the inner core without this heat source, because the temperatures required for a purely thermally driven dynamo early in Earth's history are unreasonably high (Nimmo, 2015). This problem has become even more pressing as recent calculations (de Koker et al., 2012; Pozzo et al., 2012, 2014) and experiments (Gomi et al., 2013; Seagle et al., 2013; Ohta et al., 2016) have shown that the thermal conductivity of iron and iron alloys at outer core conditions could be 2–3 times higher than formerly believed, although uncertainty persists on this issue (Konôpková et al., 2016). If a radiogenic heat source were present, the core would cool more

* Corresponding author.
*E-mail address:* chidesterba@uchicago.edu (B.A. Chidester).

http://dx.doi.org/10.1016/j.gca.2016.11.035
0016-7037/

slowly, the inner core would be somewhat older, and the inferred initial temperature of the core would be more reasonable. It has been suggested that the extremely high temperature conditions of core formation could cause even highly lithophile elements such as Mg to partition into the metallic core (Badro et al., 2016; O'Rourke and Stevenson, 2016). This leads one to reconsider whether other lithophile elements such as U, Th, K, and rare-earth elements (REE) might also partition into the core in significant amounts, and thus, explain isotopic deviations of REE in surface rocks with respect to the chondritic building blocks of the planet (e.g. Boyet and Carlson, 2005).

Previous high-pressure, high-temperature metal–silicate partitioning experiments have shown that U will partition into the metallic phase at very low oxygen fugacity ($fO_2$) and high S content, but that under the $P$–$T$–$fO_2$ conditions of Earth's upper mantle, the partitioning is too low for U to be an important heat source in the core (Malavergne et al., 2007; Bouhifd et al., 2013). However, these experiments were done at relatively low pressures and temperatures (i.e. $P \leqslant 20$ GPa and $T \leqslant 2700$ K). To match the mantle abundances of the siderophile elements such as Ni and Co, equilibration of the metal in a magma ocean would have had to take place at much deeper conditions on average (i.e. $P$ between 30 and 60 GPa, with $T$ up to 4200 K) (Li and Agee, 2001; Bouhifd and Jephcoat, 2011; Siebert et al., 2012; Fischer et al., 2015; Righter et al., 2016). Wohlers and Wood (2015) recently suggested that a significant amount of U (and other nominally lithophile elements) could have partitioned into sulfides at very reducing conditions in the solar nebula, and that by incorporating those sulfides into the growing core early in planetary accretion, those elements would have been trapped in the core even as the whole planet was continuously becoming more oxidized and S-depleted. That model relies on a very specific scenario for planetary growth, and it is necessary to consider more broadly the conditions under which heat-producing elements could have entered the core as the planet was growing. Thus, it is important to investigate the partitioning of U at higher pressures and temperatures such that the partitioning behavior of U can be investigated within the $P$–$T$ space of a deep magma ocean. Here, we demonstrate that under magma ocean conditions, U becomes less lithophile, and could have altered the energy budget of the core if equilibration in a magma ocean occurred at very high temperatures.

## 2. EXPERIMENTAL METHODS

### 2.1. Sample preparation and laser heating

Metal–silicate partitioning experiments were conducted in the laser-heated diamond anvil cell (LH-DAC) at the University of Chicago. The silicate used in most experiments was a mixed oxide powder having a major element composition of pyrolite (with or without Ca) (McDonough and Sun, 1995), but without any FeO to keep conditions as reducing as possible, and with elevated levels of $UO_2$ to facilitate analysis of the experimental products (Table 1). In two cases (B22 and B23) the silicate was composed of a mixture of $UO_2$, $ThO_2$, and $SiO_2$. MgO (99%), $Al_2O_3$ (99.99%), $SiO_2$ (99.9%), $CaSiO_3$ (meta, reagent grade), Fe (99.9+%, <10 μm), FeSi (99.9%), and FeS (99.9%) were all purchased from Alfa Aesar. To remove any contaminating OH from the oxide and silicate powders, they were fired in a furnace at 1000 °C for 12–20 h prior to use. $ThO_2$ (99.99%) was purchased from Strem Chemical. Depleted $UO_2$ powder was purchased from SPI Chemical. This material contained a small amount of polymer binder, so it was washed in ethanol and baked at 100 °C prior to sample preparation. The silicate and oxide materials were mixed together in the proportions shown in Table 1, and ball-milled in a tungsten carbide (WC) capsule at 20 Hz for 1.5 h. The metal used in these experiments was either stoichiometric FeSi or a mixture of FeSi, FeS, and Fe, to produce Fe alloys of targeted compositions during the experiment. The metals were also blended in a WC capsule using a ball mill at 20 Hz for 1.5 h. Tungsten was not detected in any of the samples; however, it is possible that trace W was introduced during the ball milling processes and that it was not observed as a result of a strong peak overlap between W and Si using energy dispersive analytical techniques.

Oxygen fugacity is not controlled externally in laser heated diamond anvil cell experiments; this is precluded by the nature of the experiments (~10 μm × 30 μm diameter laser heated spot, confined between diamond anvils). Similarly, due to the very small scale of the samples, one cannot precisely control a priori the exact proportions of metal and silicate in each sample. Here, as in previous metal–silicate partitioning experiments at very high $P$–$T$ conditions, the oxygen fugacity of the system is self-buffered by exchange of Fe and Si between metal and silicate melts. We influenced this self-buffering toward reducing conditions by using starting materials with high Si contents in the metal, but as recognized previously (Siebert et al., 2012; Fischer et al., 2015), the Fe–Si exchange reaction at high $P$–$T$ conditions drives the oxygen fugacity of the experimental products toward a relatively narrow range of ΔIW conditions. Importantly, we measure the composition of coexisting metal and silicate products to establish the $fO_2$ that was achieved in the experiments.

Diamond anvil cell samples were loaded into stainless steel gaskets pre-indented to 18–23 GPa or rhenium gaskets pre-indented to 25–28 GPa. The diamond culets measured 300 or 250 μm in diameter. The metallic sample material was pressed into a thin foil of ~2–5 μm thick, and encapsulated with flakes of silicate powder. Samples B22 and B23 were prepared as extreme end-members using a mixture of $UO_2$, $ThO_2$, and FeSi as the pressed flake and $SiO_2$ was used as the surrounding silicate. A small amount of $Al_2O_3$ was introduced in these two samples by processing in a corundum mortar and pestle. The samples were dried at 90 °C for 30–60 min after loading but prior to closing the cell to remove any adhered moisture from the sample. The pressure at the location to be heated was determined using the Raman shift of diamond (calibrated to ruby under quasi-hydrostatic conditions after Akahama and Kawamura, 2007) prior to heating. Several pressure measurements were made across each sample chamber, and

Table 1
Starting compositions in weight% for the metal and silicate portions of each sample. Samples B22 and B23 were structured in such a way that the starting composition could not be estimated in this way – see text.

| Sample # | Metal | Silicate | | | | |
|---|---|---|---|---|---|---|
| | | MgO | $Al_2O_3$ | $CaSiO_3$ | $SiO_2$ | $UO_2$ |
| B42 | FeSi | 36.56 | 8.40 | 0 | 43.44 | 11.60 |
| B49 | Fe–12S–22Si | 35.35 | 8.13 | 6.85 | 38.46 | 11.22 |
| B50 | FeSi | 35.35 | 8.13 | 6.85 | 38.46 | 11.22 |
| B56 | FeSi | 35.35 | 8.13 | 6.85 | 38.46 | 11.22 |
| B66 | Fe–4S–15Si | 35.35 | 8.13 | 6.85 | 38.46 | 11.22 |

they were found to be within 1–2 GPa on average, indicating reasonably constant stress state across the small sample chamber. Any non-hydrostatic strain is expected to be eliminated at the high temperatures of melting. Thermal pressure was estimated from two additional samples of the same geometry under the same pressure range that were laser heated with in situ synchrotron X-ray diffraction to be ~20% of the room temperature pressure (Fischer et al., 2015). The pressures listed in Tables 2 and A.1 include the 20% thermal pressure for all samples in this study. The error on pressure was determined based on uncertainties in the thermal pressure and in the diamond Raman measurement.

The laser heating system used for these experiments is a double-sided version of that described by Campbell (2008). Samples were compressed to the target pressure, then laser-heated on both sides using a 1064 nm Yb-doped fiber laser. Temperature was gradually increased to above the sample liquidus over a period of ~5 min. Samples were held at the maximum temperature for 15–30 s, then quenched to room temperature to conserve the high-temperature chemical distribution by turning off the laser. Average temperature in these experiments was measured spectro-radiometrically with 5–10 ms spectral exposures, while temperature gradients were simultaneously assessed using a four-color spectral imaging system with a 200–500 ms exposure time (Campbell, 2008).

### 2.2. Sample recovery

The samples were decompressed over ~30 min and then secured within the gasket to a 0.5″ aluminum SEM pin stub. They were then coated with a thin (~10 nm) layer of carbon to provide a conductive surface for imaging with an electron beam. The samples were sectioned along the axis of compression through the center of the laser-heated spot using a dual beam focused ion beam (FIB) at Johnson Space Center (FEI Quanta 3D FEG). The FIB sections of each sample were attached to a copper TEM grid and typically thinned to ~1 μm.

### 2.3. Chemical analysis

Chemical analysis of the samples was done at the University of Chicago using energy dispersive X-ray spectroscopy (EDX) on either a JEOL 5800LV or Tescan Lyra3 scanning electron microscope (SEM) at 15 keV and ~2 nA. Using the JEOL instrument, several profiles were taken across each sample with measurements every 0.25 μm and 2 min/step. Using the Tescan instrument, profiles were taken in 20 nm steps with a 10 ms dwell time per pixel and a total of 350 passes over the profile. Compositions were determined by averaging all of the point measurements from each respective phase. The measurements reported in this study are very precise due to a large number of measurements made in each phase. Based on measurements of analytical standards, the sample measurements are expected to be accurate to within 5% (relative), but this calibration inaccuracy is expected to be similar for both the metal and the silicate phase, so will cancel out in the partition coefficient calculations. Detection limits for Al, Ca, Mg, and U in the metallic phase were determined as 3 times the background. These measurements were made in the metallic phase of sample B59, which contained all of these elements in concentrations too low to be detected by EDX. Detection limits are dependent on the number of measurements made in each phase because of counting statistics. For the metals in the samples reported here (13–261 measurements) the range of detection limits is: 0.04–0.18 atom % Al, 0.03–0.15 atom% Ca, 0.06–0.28 atom% Mg, and

Table 2
Experimental conditions for the DAC samples. Oxygen fugacity ($fO_2$) was calculated using the mole fractions of Fe and FeO and assuming ideality. Partition coefficients ($D_U$) and exchange coefficients ($K_D$) were calculated using mole fractions.

| Sample | P (GPa) | +/− | T (K) | +/− | $fO_2$ (ΔIW) | + | − | $D_U$ | +/− | $K_D$ | +/− |
|---|---|---|---|---|---|---|---|---|---|---|---|
| B22 | 67 | 6 | 4700 | 400 | −2.1 | 0.01 | −0.01 | 0.0328 | 0.0003 | 0.00294 | 0.00005 |
| B23 | 61 | 6 | 5000 | 300 | −2.62 | 0.03 | −0.04 | 0.0441 | 0.0003 | 0.00216 | 0.00009 |
| B42 | 57 | 6 | 3800 | 200 | −2.15 | 0.05 | −0.05 | 0.039 | 0.001 | 0.0032 | 0.0002 |
| B49 | 55 | 5 | 5400 | 300 | −1.53 | 0.03 | −0.03 | 0.662 | 0.004 | 0.114 | 0.004 |
| B50 | 57 | 6 | 4800 | 300 | −3.3 | 0.2 | −0.2 | 0.23 | 0.01 | 0.005 | 0.001 |
| B56 | 41 | 5 | 4000 | 200 | −3.19 | 0.02 | −0.02 | 0.042 | 0.002 | 0.00107 | 0.00005 |
| B66 | 54 | 5 | 4400 | 300 | −2.12 | 0.06 | −0.07 | 0.23 | 0.004 | 0.02 | 0.002 |

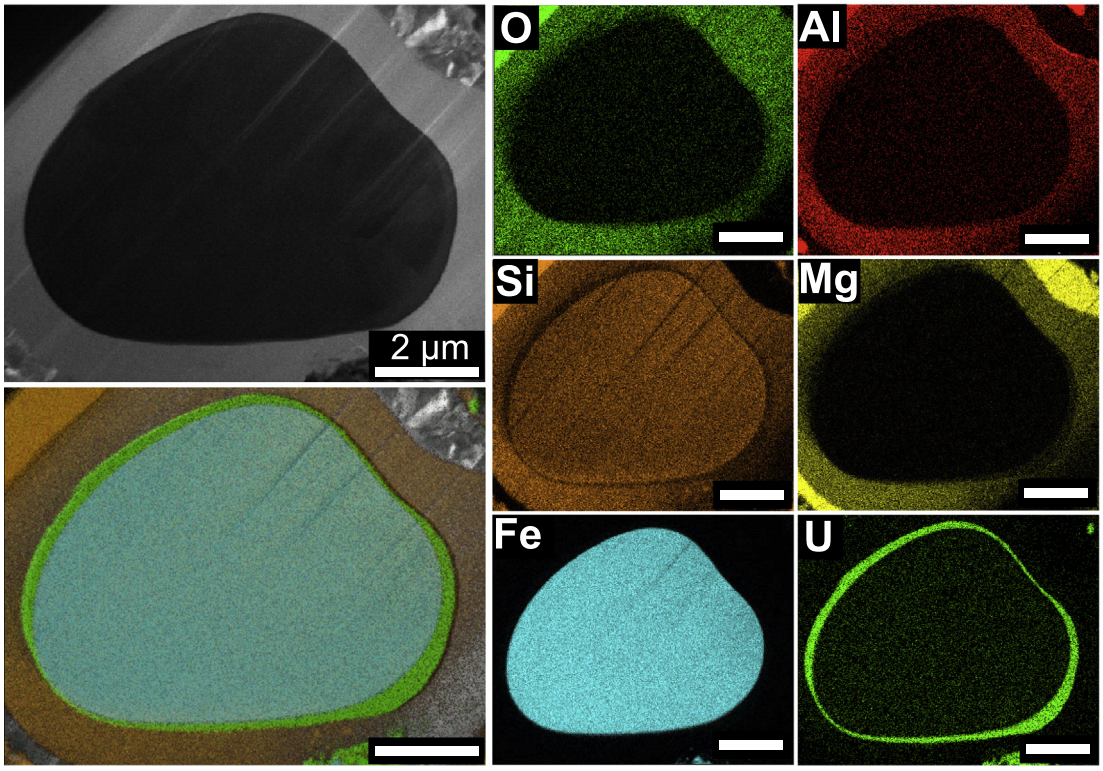


Fig. 1. (Top left) Transmission electron image of sample B42, recovered from 57 GPa and 3800 K. The dark region contains metallic and silicate melts; the bright region is amorphous $MgSiO_3$ that was bridgmanite under high P conditions. (Bottom left) Composite X-ray map of Fe, U and Si. (Right) X-ray maps for individual elements.

0.02–0.09 atom% U. X-ray maps of select elements were obtained for sample B42 (Fig. 1) using the JEOL 2500SE field emission scanning transmission electron microscope (STEM) at Johnson Space Center.

In several cases, the silicate melt region was small compared to the activation volume of the EDX measurements. In these cases, we were able to deconvolute the signals from each phase using a point-spread function. Each point measurement was treated as an integration over an area having a Gaussian-weighted signal, and the composition of the silicate melt was fitted to a line profile across each phase (Fig. A.1). Other fitted parameters in this analysis included the location of the boundary between the silicate and metallic melt phases, the width of the Gaussian ($\sigma$), and if necessary, the composition of the silicate mineral in the outer region of the laser heated spot. The Mathematica code and example data are provided (ExamplePSA.nb and ExamplePSA_data.csv in the Supplementary Information). For those samples whose compositions were fit in this way, the uncertainties provided are the standard errors to the fit.

Because the samples were thinner than the activation volume of the EDX measurement, the analyses were normalized to 100%. Oxide mole fractions in the silicate melt were calculated stoichiometrically using the following oxidation states: 6+ for S; 4+ for Si and Th; 3+ for Al; and 2+ for Fe, Mg, Ca and U (See Section 4.1). Oxygen measurements in Fe-rich alloys are often challenging using EDX because of a slight overlap in excitation energy between the O $K\alpha$ line (0.525 keV) and the Fe $L\alpha$ line (0.705 keV), but it is known that a significant amount of O will partition into Fe metals at high $P$–$T$ conditions (Frost et al., 2010; Fischer et al., 2015), so it is necessary to obtain accurate O contents in the metals in these experiments. The Tescan system at the University of Chicago is equipped with a silicon-drift detector (Oxford Instruments X-Max$^N$) that has sufficient energy resolution to fully deconvolute these Fe and O peaks. Measurements on several Fe-bearing silicate and oxide standards on this instrument showed the O measurements to be accurate to within 5% (relative). Furthermore, there was no significant difference in the silicate melt compositions of our samples when they were calculated as stoichiometric oxides or when measuring O as a separate element. Finally, the oxygen content in the metal phase of each sample was compared to the expected O content from the published $P$–$T$ dependence of O partitioning between peridotite and metal (Fischer et al., 2015), and most were found to be within 15% of those predicted values. Samples B42, B50 and B56 were not measured using the silicon-drift detector, so the reported metal compositions for these samples were obtained by measuring all elements except O in the EDX, and renormalizing with the O content predicted by the O partitioning parameters at the relevant $P$–$T$ conditions (Fischer et al., 2015).

## 3. RESULTS

### 3.1. Sample texture

Metal–silicate partitioning samples were sectioned to ~1 μm thick for observation in the SEM. Figs. 1 and 2 show representative samples after sectioning. The samples always consisted of a quenched round metal melt ball surrounded by a quenched silicate melt. There was a region of silicate material, often of bridgmanite composition, outside the silicate melt that was clearly recrystallized during heating. The laser-heated spots were on the order of 20 μm in diameter. There was no evidence of immiscible metallic phases, in contrast to the Fe–S–Si miscibility gap observed below 15 GPa (Sanloup and Fei, 2004). The metal phase often exhibited a uniform quench texture, where Si and O that were soluble in the metal at high temperature exsolved upon rapid cooling. Due to the rapid quench rates in the diamond anvil cell, no strong quench texture was observed in the silicate melt. That the boundaries between each phase (metallic melt, silicate melt and silicate mineral) were always smooth and continuous is evidence that the system within the laser-heated spot had a minimal free energy, i.e. was locally equilibrated under the high $P$–$T$ experimental conditions. Further demonstration of local equilibrium was that the composition of the silicate was uniform over sample regions of different scales, indicating that kinetic processes like thermal diffusion were not a problem.

### 3.2. Chemical composition and oxygen fugacity

The pressure, temperature, and relative $fO_2$ conditions of each sample from this study are listed in Table 2, and together with all literature data used in this study in Table A.1. The compositions of each phase of each sample in this study and their errors are reported in Table 3 (metal phase) and Table 4 (silicate phase) and are provided as text files (Tables A.2 and A.3) in the Supplemental Material for ease of use. Here, $fO_2$ was calculated in reference to the iron-wüstite buffer assuming ideality (i.e. that the activities of Fe in the metal and FeO in the silicate were equal to their mole fractions in their respective phases), such as:

$$\Delta IW = 2\log_{10}\left(\frac{X_{FeO,silicate}}{X_{Fe,metal}}\right) \quad (1)$$

To evaluate the effect of the high concentrations of Si and O in the metal phases of our samples, we also calculated this parameter using the activity of Fe ($a_{Fe}$) from the online metal activity calculator (http://www.earth.ox.ac.uk/~expet/metalact/; based on Wade and Wood, 2005) in place of $X_{Fe,metal}$. This calculator failed to compute a result for several of our samples at very high temperatures. However, thermodynamic results using the model activities that were possible to compute were virtually unchanged using this model, except that the residuals to the fit appeared to trend slightly with temperature. Thus, we conclude that this type of model is not yet calibrated to sufficiently high temperatures for this study, and for now unnecessary given other uncertainties in our experiments.

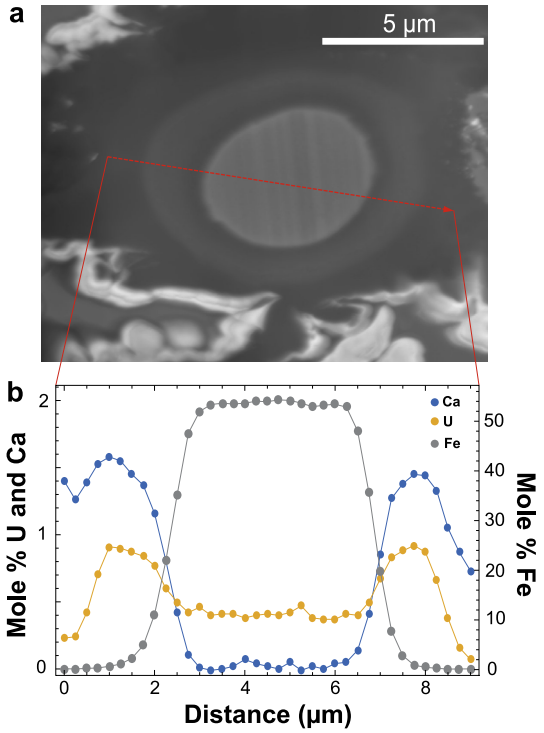


Fig. 2. (a) Back-scattered electron image of sample B50. Sample recovered from 56 GPa and 4700 K. Red arrow indicates location of EDX profile. (b) EDX profiles of U, Ca and Fe across sample B50. Measurements were made in 0.25 μm steps. (For interpretation of the references to colour in this figure legend, the reader is referred to the web version of this article.)

For consistency, the literature values for $fO_2$, as well as partition and exchange coefficients, were recalculated using mole fractions of elements and oxides converted from the weight percents reported.

As mentioned previously, compositions of each phase were obtained from point measurements in profile across the laser-heated spot. An example of this type of measurement is given in Fig. 2. In all cases, U was measurable in the silicate melt and within the metallic region, but was usually not measurable in the crystalline bridgmanite outside of the melt region. This demonstrates very low compatibility of U in crystalline bridgmanite (Corgne et al., 2005), as well as the significant partitioning of U into Fe metal at these high pressures and temperatures. It is notable that Th was present at relatively high levels in two of the experiments listed here, B22 and B23, but was not measurable in the metallic phase of either sample. This indicates a dichotomy between the chemical behaviors of Th and U, which are otherwise quite similar.

It can be seen in Fig. 2b that in sample B50, recovered from 56 GPa and 4700 K, both U and Ca concentrate in the silicate melt, and that U partitions into the metal but Ca does not. A concern raised for measurement of metal–silicate partitioning samples from the laser-heated diamond anvil cell is that the spatial scale is too small, and the measurement is contaminated with fluorescence from a higher abundance region (Wade and Wood, 2012). In this regard, comparison of U chemical profiles with those of Ca is par-

Table 3
Metal phase compositions in both mole percent and weight percent for the samples in this study. Standard errors are given on the least significant digit. "*n*" is the number of measurements. Asterisks indicate oxygen contents that were calculated rather than measured – see text. If an element was below the detection limit, it is denoted as "nd". Elements with 0 percent were not present in the sample material. Ca and Th are not included in this table because they were not detectable by EDX in any of the metallic phases of the samples studied.

| Sample | Fe | Si | O | S | Al | Mg | U | *n* |
|---|---|---|---|---|---|---|---|---|
| B22 mol% | 57.27(5) | 33.04(4) | 8.34(5) | 0 | nd | 0 | 1.36(1) | 261 |
| wt% | 69.78(6) | 20.25(2) | 2.9(2) | 0 | nd | 0 | 7.06(5) | |
| B23 mol% | 47.16(5) | 42.51(4) | 8.65(5) | 0 | 0.1(1) | 0 | 1.54(1) | 91 |
| wt% | 60.75(6) | 27.54(3) | 3.19(2) | 0 | 0.06(6) | 0 | 8.45(5) | |
| B42 mol% | 48.7(1) | 44.6(1) | 5.26* | 0 | 0.23(2) | 0.76(7) | 0.45(1) | 13 |
| wt% | 64.9(1) | 29.91(7) | 2.01* | 0 | 0.15(1) | 0.44(4) | 2.56(6) | |
| B49 mol% | 33.4(4) | 18.31(2) | 21.28(6) | 19.84(3) | 0.949(8) | 2.92(1) | 3.299(8) | 126 |
| wt% | 44.01(5) | 12.14(1) | 8.03(2) | 15.01(2) | 0.605(5) | 1.675(6) | 18.53(4) | |
| B50 mol% | 57.7(1) | 37.29(8) | 2.54* | 0 | 0.75(2) | 1.24(8) | 0.439(5) | 29 |
| wt% | 72.2(1) | 23.46(5) | 0.91* | 0 | 0.45(1) | 0.68(4) | 2.34(3) | |
| B56 mol% | 50.4(6) | 47.22(6) | 1.93* | 0 | 0.2(1) | 0.1(1) | 0.122(5) | 151 |
| wt% | 66.89(8) | 31.50(4) | 0.73* | 0 | 0.13(6) | 0.06(6) | 0.69(3) | |
| B66 mol% | 66.36(8) | 8.30(2) | 19.51(7) | 3.89(2) | 0.30(1) | 1.06(3) | 0.580(8) | 40 |
| wt% | 81.36(8) | 5.13(1) | 6.86(2) | 2.74(1) | 0.18(1) | 0.57(2) | 3.04(4) | |

Table 4
Silicate melt compositions in both mole percent and weight percent. Errors are either the standard errors of the average or the error from the point spread analysis. Elements with 0 percent were not present in the sample material. †Either the number of measurements or "PS" indicating a fit using the point spread function.

| Sample | MgO | $AlO_{1.5}$ | $SO_3$ | $SiO_2$ | CaO | FeO | $ThO_2$ | UO | *n*† |
|---|---|---|---|---|---|---|---|---|---|
| B22 mol% | 0 | 8.89(6) | 0 | 39.46(9) | 0 | 5.13(8) | 5.16(3) | 41.37(7) | 251 |
| wt% | 0 | 3.01(2) | 0 | 15.74(4) | 0 | 2.45(4) | 9.04(5) | 69.8(1) | |
| B23 mol% | 0 | 7.63(8) | 0 | 45.8(1) | 0 | 2.31(9) | 9.44(5) | 34.82(9) | 57 |
| wt% | 0 | 2.66(3) | 0 | 18.79(4) | 0 | 1.13(4) | 17.02(9) | 60.4(2) | |
| B42 mol% | 28.4(2) | 13.7(1) | 0 | 42.0(2) | 0 | 4.1(2) | 0 | 11.7(1) | PS |
| wt% | 15.0(1) | 9.15(7) | 0 | 33.1(2) | 0 | 3.9(2) | 0 | 38.9(3) | |
| B49 mol% | 40.5(1) | 10.5(1) | 4.9(1) | 31.6(1) | 1.85(2) | 5.8(2) | 0 | 4.98(3) | PS |
| wt% | 26.14(6) | 8.57(8) | 6.3(1) | 30.4(1) | 1.66(2) | 6.7(2) | 0 | 20.3(1) | |
| B50 mol% | 48.72(9) | 17.9(4) | 0 | 27(2) | 3.15(5) | 1.2(3) | 0 | 1.94(9) | PS |
| wt% | 37.38(7) | 17.4(4) | 0 | 31(2) | 3.36(5) | 1.6(4) | 0 | 9.4(4) | |
| B56 mol% | 33.59(3) | 9.03(3) | 0 | 49.47(4) | 3.73(2) | 1.28(3) | 0 | 2.90(1) | 79 |
| wt% | 23.25(2) | 7.90(3) | 0 | 51.03(4) | 3.59(2) | 1.58(4) | 0 | 12.65(4) | |
| B66 mol% | 43.6(2) | 8.98(7) | 2.13(3) | 35.7(1) | 1.32(2) | 5.8(4) | 0 | 2.52(2) | PS |
| wt% | 31.0(1) | 8.09(6) | 3.01(4) | 37.9(1) | 1.31(2) | 7.4(5) | 0 | 11.31(9) | |

ticularly important. Ca and U have similar absorption energies in EDX (3.164 and 3.690 kV for the U $M\alpha$ line and the Ca $K\alpha$ line, respectively); thus, if the measurements in the metal were artificially high due to fluorescence from the silicate, we would expect to see it with both elements, but this is not observed. Indeed, the apparent abundance of U in the silicate mineral directly outside the silicate melt is lower than that measured in the metal. We conclude that secondary fluorescence has not compromised our measurements of U in the metal phase in these experiments.

## 4. DISCUSSION

### 4.1. Thermodynamic Modeling and the oxidation state of U

Partition coefficients for U between metal and silicate were calculated as

$$D_{\mathrm{U}} = \frac{X_{\mathrm{U,metal}}}{X_{\mathrm{UO}_{n/2},\mathrm{silicate}}} \tag{2}$$

where $X_i$ are the mole fractions of those species in their respective phases and $n$ is the oxidation state of the U cation in the silicate melt. The partition coefficient is not only dependent on thermodynamic variables such as temperature and pressure, but also on composition and the $fO_2$ of the system. Because of this, a multivariate approach is necessary to address all of the variables simultaneously. The dependence on redox condition is best described by considering the exchange reaction

$$\mathrm{UO}_{n/2} + \frac{n}{2}\mathrm{Fe} \leftrightarrow \frac{n}{2}\mathrm{FeO} + \mathrm{U} \tag{3}$$

in which uranium (having valence $n$) is reduced to a metal by exchanging oxygen with iron, the most abundant multivalent element in Earth's interior. The exchange coefficient for this reaction,

$$K_{\mathrm{D}} = \frac{X_{\mathrm{U}}/X_{\mathrm{UO}_{n/2}}}{(X_{\mathrm{Fe}}/X_{\mathrm{FeO}})^{n/2}} = \frac{D_{\mathrm{U}}}{(D_{\mathrm{Fe}})^{n/2}} \tag{4}$$

is thus a useful means of describing the dependence of U partitioning on $P$, $T$, and composition of the various phases independent of the redox state. However, use of the exchange coefficient requires that the oxidation state of U be assumed or inferred from the fit to the data. Previous studies (Malavergne et al., 2007; Bouhifd et al., 2013) have inferred a U oxidation state of 4+, which is reasonable given that the most reduced form of U at surface conditions is 4+. However, this assumption did not work well for fitting the combined high-pressure and low-pressure data here.

When fitting the dependence of partition coefficient ($D_U$) on $fO_2$ explicitly, as in Eq. (5),

$$\log_{10} D_U = a + \frac{b}{T} + c\frac{(1-X_S)^2}{T} + d\frac{(1-X_{SiO_2})^2}{T} + e\Delta IW \quad (5)$$

we find that the U oxidation state within the silicate liquid at these conditions is best described as 2+, instead of the 4+ valence that has previously been inferred. Here, $X_i$ is the mole fraction of species $i$, and $a$ and $b$ are representative of the entropy and enthalpy of the reaction in Eq. (3), respectively. The compositional terms are expressed as the excess Gibbs free energy of mixing in a Guggenheim-type binary mixing model (e.g. Ganguly, 2009), where the log of the activity coefficient ($\gamma_i$) equals a constant times $(1 - X_i)^2/T$. Eqs. (5) and (6) neglect any and all terms that were found to be statistically insignificant to the partitioning of U, including pressure and other compositional effects, discussed later. In this notation, the coefficient $e$ is equal to negative one quarter of the U oxidation state in the silicate liquid. The parameters for this fit are listed in Table 5, where $e = -n/4 = -0.49$. Thus, the inferred oxidation state, $n$, for U in the silicate melt is 2+. To show this result more explicitly, we corrected all of the data using the fitted parameters in Eq. (5) to single temperature (3000 K), S content in the metal (2 wt%) and $SiO_2$ content in the silicate (0.45 wt%). These data were then plotted in Fig. 3 as corrected $\log_{10}D_U$ versus the measured ΔIW values. The slope of this line is indeed −0.49, consistent with $U^{2+}$. A line with slope of −1 (indicating a 4+ oxidation state for U) is also shown for reference. The data used in this regression are listed in Table A.1.

This surprising result has only been previously observed using relatively exotic organometallic synthesis methods (MacDonald et al., 2013) and is consistent with recent

Table 5
Metal–silicate partitioning parameters fit to Eqs. (5) and (6) for U. The root-mean-square (RMS) misfit to the data is 0.31 log units in both cases. The data ($n = 20$) are listed in Table A.1.

| | Eq. (5) | | Eq. (6) | |
|---|---|---|---|---|
| Parameter | Value | Error (±) | Value | Error (±) |
| $a$ | 0.10 | 0.3 | 0.10 | 0.3 |
| $b$ | −11,000 | 1000 | −11,000 | 1000 |
| $c$ | −4700 | 900 | −4700 | 800 |
| $d$ | 13,000 | 3000 | 13,000 | 3000 |
| $e$ | −0.49 | 0.07 | – | – |

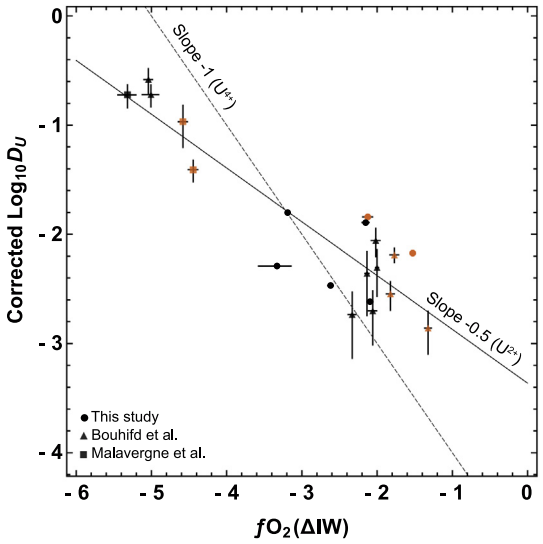


Fig. 3. Plot of partition coefficients as a function of $fO_2$(ΔIW). Orange symbols are sulfur-containing samples. All of the data have been corrected to 3000 K with 2 wt% S in the metal and 45 wt% $SiO_2$ in the silicate melt. Lines of slope −1 (indicating $U^{4+}$) and −0.5 (indicating $U^{2+}$) are included for reference. (For interpretation of the references to colour in this figure legend, the reader is referred to the web version of this article.)

papers that have reported a reduction in oxidation state of two other high-field strength elements, Nb and Ta, in silicate melts at 5 GPa under reducing conditions (Cartier et al., 2014, 2015). These results indicate that metal–silicate partitioning of these elements is less dependent on $fO_2$ at high $P$–$T$ conditions. This change in U valence could explain the difference in partitioning behavior between U and Th in the two experiments that contain both elements. This is also likely important for mineral–melt partitioning of these elements at depth within the Earth, as cations with lower field strength are more likely to be compatible in mantle minerals (Blundy and Wood, 2003). We propose that this could be a mechanism for fractionation between U and Th at high $P$–$T$ conditions and should be investigated further.

### 4.2. Comparison with previous data

A comparison of our high-pressure exchange coefficients to earlier work (Malavergne et al., 2007; Bouhifd et al., 2013) in Fig. 4 shows a strong dependence of $K_D$ on temperature. This dependence was not discernable in earlier studies, likely because of the relatively small pressure and temperature ranges previously investigated. Much of the scatter in Fig. 4 relates to other factors, besides temperature, that affect the metal–silicate partitioning of U. To parse the dependence of partitioning on pressure, temperature and chemical composition of the metal and the silicate, the $K_D$ data were fit to an equation of the form

$$\log_{10} K_D = a + \frac{b}{T} + c\frac{(1-X_S)^2}{T} + d\frac{(1-X_{SiO_2})^2}{T} \quad (6)$$

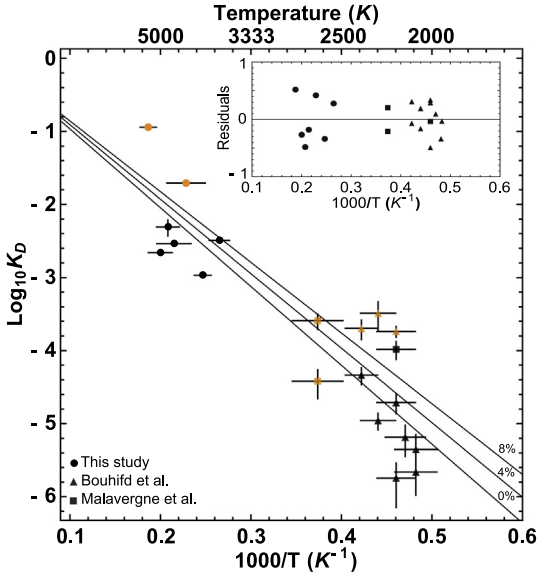


Fig. 4. Temperature dependence of metal–silicate partitioning of U. Orange symbols are sulfur-containing samples. Solid lines represent the expected exchange coefficients at constant sulfur content in the metal in weight percent. Inset: Residuals to the fit. (For interpretation of the references to colour in this figure legend, the reader is referred to the web version of this article.)

where the coefficients are thermodynamically equivalent to those in Eq. (5), except that the $fO_2$ term is accounted for in $K_D$. These coefficients are listed in Table 5, and are found to be identical to those in Eq. (5).

Our results show that, within the range of conditions appropriate to core formation in Earth, temperature is the factor that most strongly influences metal–silicate partitioning of uranium. Sulfur in the core appears to be favorable for U partitioning into the metal, while $SiO_2$ in the silicate has a strong negative effect. In this context, $SiO_2$ content of the silicate melt is a proxy for how polymerized the melt is, which is often a consideration in partitioning studies at lower pressures and temperatures (O'Neill and Eggins, 2002; Righter, 2003). The effect of pressure was found to be insignificant, and is not included in the reported parameterization.

The concentrations of $UO_2$ in the silicate melts of these samples are far greater than the very low (ppb to ppm) levels that occur in natural silicates. This was necessary, as the available techniques for measuring composition at such high spatial resolution do not have the capability of detecting elements at such low concentrations. Consequently, it is important to consider that these samples may not fall within the Henry's Law range of chemical activity; i.e. the activity of U, and therefore its partitioning behavior, is different (either higher or lower) than it would be in nature. This would be accounted for in the thermodynamic model in the same way that we have accounted for S and $SiO_2$, with a coefficient on the composition term to describe the non-ideality of the solution. Despite the range of $UO_2$ (or U) concentrations in the silicate (or metal), it was found that such a term was not statistically significant. Thus, we concluded that the high concentrations of $UO_2$ in our samples do not affect the observed partitioning of U. Likewise, it was found that additional terms in Eqs. (5) and (6) to account for the Si content for the metal were also not significant. Thus, the activity coefficients of $UO_2$ and Si appear not to vary strongly over the range of compositions explored in this study, and we tentatively conclude that Henry's Law violations do not impact our results. Further examination of this issue would benefit from trace elemental analyses, probably on multianvil press or piston-cylinder experiments.

In all the experiments described here, as well as many of those reported in the literature, the metallic phase has the opportunity to be completely saturated in carbon due to reaction with the sample containment (either graphite capsules in multi-anvil or piston cylinder press, or diamonds in the diamond anvil cells). Unfortunately, in addition to being a ubiquitous environmental contaminant, C is difficult to measure using the spectroscopic techniques described here. However, there is very little evidence that C is actually an important factor for metal–silicate partitioning of U. The interaction parameter between C and U in a C-saturated iron alloy is listed in the Steelmaking Data Sourcebook as 0 at temperatures around 1600–1700 K (Japan Society for the Promotion of Science and the 19th Committee on Steelmaking, 1988). Furthermore, Bouhifd et al. (2013) completed metal–silicate partitioning experiments of U at moderate pressures in both MgO and graphite capsules and found C to have a negligible effect. They, along with others (Miettinen, 1998; Kawanishi et al., 2009; Li et al., 2015), show that the C and Si contents of the metallic phase are inversely correlated. Thus, given the high Si contents of the metals in our study, and the negligible interaction between U and C, we expect our parameterization to be accurate without including a parameter for the effect of C content.

### 4.3. Core formation at a single effective pressure and temperature

We use this parameterization of U partitioning with a differentiation model to place bounds on the U content of the Earth's core. Using average $P$–$T$ conditions of core-mantle equilibration (Siebert et al., 2012; Fischer et al., 2015), that is $P = 45$–$58$ GPa and $T = 3900$–$4200$ K (the liquidus of peridotite from Fiquet et al. (2010)), with the core and mantle composition from McDonough, 2003 (i.e. a conservative 2 wt% S in the core, 45 wt% $SiO_2$ and a current 20.3 ppb U in the bulk silicate Earth (BSE)), and assuming an $fO_2$ of IW-2, we calculate partitioning of U in the differentiating planet to be $D_U = 0.026$ (+0.03/−0.01) to 0.040 (+0.04/−0.02), resulting in a concentration of 1.4–2.1 ppb U in the core. It is important to note that these calculations were done for the age 4.5 Ga. Starting with a current 20.3 ppb U in the BSE and integrating back through time, the U content in the initial BSE equaled 53.7 ppb. This U concentration in the core would produce a modest 0.6–0.9 TW of heat at the onset of core

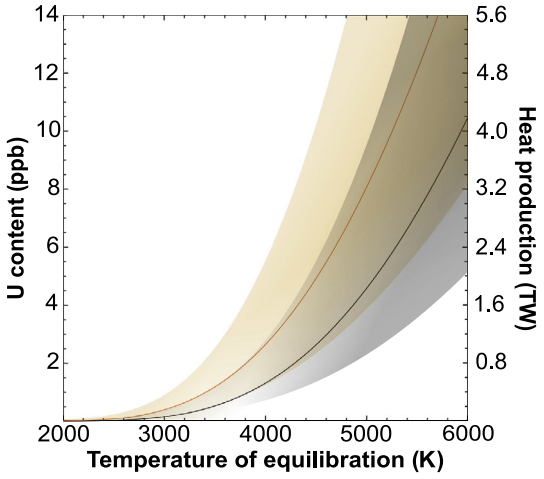


Fig. 5. U content and the resulting heat production at the onset of core formation as a function of metal–silicate equilibration temperature. Black line: 0 wt% S in the metal; orange line: 8 wt% S. Error envelopes are derived from the root-mean-squared error on the fit. (For interpretation of the references to colour in this figure legend, the reader is referred to the web version of this article.)

formation, and 0.10–0.15 TW at the present time (Turcotte and Schubert, 2002).

Additionally, we confirm the strong dependence of U partitioning on S content of the core discussed by previous studies (Malavergne et al., 2007; Bouhifd et al., 2013; Wohlers and Wood, 2015). Raising the sulfur content of the metal to an extreme upper bound of 8 wt% elevates the amount of U initially partitioned into the core at an average temperature of 4200 K to 3.5 (+3/−1) ppb, corresponding to 1.4 TW of heat. We emphasize, however, that high sulfur contents are not necessary to produce a significant radiogenic heat source by partitioning U into the core; high $P$–$T$ conditions alone can achieve this. Fig. 5 shows the amount of U partitioned into the metal as a function of temperature of metal–silicate equilibration with 0 and 8 wt% S. The amount of U in the core increases dramatically above 4000 K, temperatures that would be expected subsequent to a large impact (Canup et al., 2015) or in a basal magma ocean (Fiquet et al., 2010). The expected amount of U in the core is less if the calculations are done using the liquidus of Andrault et al., 2011, because their preferred temperature profile is lower than that of Fiquet et al., 2010. For example, using 3400 K, the liquidus temperature at 58 GPa from Andrault et al., 2011, and 2 wt% S, 0.6 ppb U is expected in the core, about 50% that using the higher liquidus profile.

### 4.4. Core formation under a range of pressures and temperatures

Modeling core formation at a single representative pressure and temperature, as above, is useful for comparison between partitioning studies, as well as for direct observation of the effects of the various fitting parameters. However, the compositions of the core and mantle were set under a range of equilibrium conditions, so it is more rigorous to model core formation as a series of equilibration steps of evolving conditions. We performed a "growing-Earth" model as described in Fischer et al., 2015, but used the liquidus profile of Fiquet et al. (2010) and added S to the core, for consistency with the single $P$–$T$ model above. Two starting compositions were used: a "reduced Earth" and an "oxidized Earth". For the reduced Earth, the initial $fO_2$ was set at IW-3.5, which evolved via high $P$–$T$ reactions to IW-1.77 at the conclusion of growth. The oxidized Earth started at IW-1.5 and evolved to IW-1.24. The U parameterization from Eq. (5) was added to this model, along with the parameterizations found in Table 2 of Fischer et al., 2015. As expected, the results of both the reduced and oxidized models are similar to our single $P$–$T$ case. A reduced Earth with 2–8 wt% S in the core would result in 1.9–3.0 ppb U, or 0.75–1.2 TW, in the core. The oxidized case with the same S content would result in 1.5–2.3 ppb U, or 0.59–0.91 TW.

### 4.5. Implications

Based on these results, U could have been an important heat-producing element in the core throughout geologic time, especially with additional contributions from K and/or Th. Given the large uncertainties in core energy and entropy models (Nimmo, 2015), it is difficult to say precisely how important this radiogenic heat source would be. The models agree that radiogenic heat contributes to the energy budget, but that it is an inefficient source of entropy available to drive the magnetic field. The high core mantle boundary (CMB) heat flow required for a thermally driven dynamo results in a very young inner core, likely less than 1 Gyr. Integrating back through time, the high heat flow would derive from very high CMB temperatures, and therefore result in extensive to complete mantle melting through much of Earth's history. A radioactive heat source would allow the inner core to be somewhat older. Most importantly, this heat source would make the early CMB temperature lower, which would curb mantle melting. Using our maximum U in the core, resulting from partitioning at 4200 K and with 8 wt% S in the core (3.5 ppb), the CMB temperature would be ~50 K lower. The large dependence on equilibration temperature is such that if the core were to differentiate at an average condition of 6000 K, the CMB temperature would be ~220 K lower. Thus, unless the core differentiated at very high temperatures or there is an additional radioactive heat source such as K, there was likely widespread melting in the lower mantle. An interesting result is that without a radiogenic heat source in the core, early widespread lower mantle melting, along with the strong incompatibility of radioactive elements in mantle minerals, would likely concentrate significant amounts of radioactive elements at the CMB. A concentrated heat source in this region would significantly affect the heat

budget of the core and mantle by lowering the heat flux out of the core, but would probably not assist in driving the magnetic field (Nimmo, 2015). Additionally, metal and silicate equilibration at these very high temperatures in the lowermost mantle would further promote addition of U to the core; the implication of not having a radiogenic heat source in the core is that the resultant high temperatures would cause a greater amount of radiogenic heat producing elements in the core.

## 5. CONCLUSIONS

We have completed metal–silicate partitioning experiments on U at pressures between 41 and 67 GPa and up to 5400 K, higher $P$–$T$ conditions than have previously been reported, and exceeding the mean conditions at which Earth's core formed. The experiments were performed at a range of $fO_2$ states, from IW-3.3 to IW-1.5. We found that U becomes significantly more siderophilic at high temperatures and S contents, such that it could have been an important heat source in the energy and entropy budget of the early core. Differentiation at mean conditions of 58 GPa, 4200 K and 8 wt% S in the metal (an extreme end-member composition) would result in a maximum of 1.4 TW of heat, which would reduce the CMB temperature by ~50 K 4.5 billion years ago. Increasing the temperature of differentiation to 6000 K, such as after a large impact, would increase the U content in the core substantially such that the CMB temperature would be reduced by 220 K. However, there was likely still wide spread melting in the lower mantle. In this vein, exsolution of MgO or $SiO_2$ as proposed by O'Rourke and Stevenson (2016) may prove to be the energy source that explains the geomagnetic field without mantle melting in the early core energy models. Additionally, we infer a reduction in the oxidation state of U to 2 + in high-pressure silicate melts, which has not been observed previously in natural samples. A lower valence could enhance the partitioning of U into the core at these extreme conditions. It would also likely affect mineral–melt partitioning of U and may result in a fractionation between U and Th at lower mantle conditions. These results lead the way for other studies of this type on lithophilic elements including K, Th, REEs, and Mg, all of which would have important implications for the geochemistry and thermal history of the planet if found to be present at significant levels in the core.

## ACKNOWLEDGMENTS

This work was funded by a NSF Graduate Research Fellowship Grant #DGE-1144082, NSF Grant #EAR-1427123, and an RTOP through the NASA Cosmochemistry Program. The FIB and TEM work were completed in the Electron Beam Analysis Labs within the Astromaterials Research and Exploration Science office at Johnson Space Center. The authors thank four anonymous reviewers and the associate editor, Munir Humayun, for helpful comments. B.A.C. thanks R. Fischer, N. Dauphas and D. Heinz for helpful discussions.

## APPENDIX A

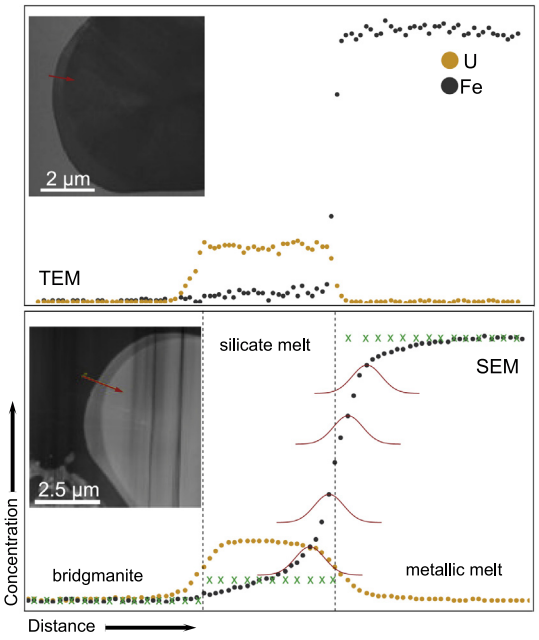


Fig. A1. Illustration of signal deconvolution of the Fe signal in each phase using point-spread analysis. For comparison of spatial resolution, top panel was measured on the TEM at Johnson Space Center; bottom panel are measurements from the Tescan SEM at the University of Chicago. Filled circles are the measurements, green x's are the fitted compositions of Fe in each phase, dashed lines are the fitted boundaries between phases. (For interpretation of the references to colour in this figure legend, the reader is referred to the web version of this article.)

## APPENDIX B. SUPPLEMENTARY DATA

Supplementary data associated with this article can be found, in the online version, at http://dx.doi.org/10.1016/j.gca.2016.11.035.

## REFERENCES

Akahama Y. and Kawamura H. (2007) Diamond anvil Raman gauge in multimegabar pressure range. *High Press. Res.* **27**, 473–482.

Andrault D., Bolfan-Casanova N., Nigro G. L, Bouhifd M. A., Garbarino G. and Mezouar M. (2011) Solidus and liquidus profiles of chondritic mantle: implication for melting of the Earth across its history. *Earth Planet. Sci. Lett.* **304**, 251–259.

Japan Society for the Promotion of Science and the Nineteenth Committee on Steelmaking (1988) *Steelmaking Data Sourcebook*, Rev. Ed. Gordon and Breach Science Publishers, New York.

Badro J., Siebert J. and Nimmo F. (2016) An early geodynamo driven by exsolution of mantle components from Earth's core. *Nature*, 1–3.

Blundy J. and Wood B. (2003) Partitioning of trace elements between crystals and melts. *Earth Planet. Sci. Lett.* **210**, 383–397.

Bouhifd M. A. and Jephcoat A. P. (2011) Convergence of Ni and Co metal–silicate partition coefficients in the deep magma-ocean and coupled silicon-oxygen solubility in iron melts at high pressures. *Earth Planet. Sci. Lett.* **307**, 341–348.

Bouhifd M. A., Andrault D., Bolfan-Casanova N., Hammouda T. and Devidal J. L. (2013) Metal–silicate partitioning of Pb and U: effects of metal composition and oxygen fugacity. *Geochim. Cosmochim. Acta* **114**, 13–28.

Boyet M. and Carlson R. W. (2005) 142Nd evidence for early (>4.53 Ga) global differentiation of the silicate. *Earth Sci. (80-.)* **309**, 576–581.

Campbell A. J. (2008) Measurement of temperature distributions across laser heated samples by multispectral imaging radiometry. *Rev. Sci. Instrum.* **79**, 15108.

Canup R. M., Visscher C., Salmon J. and Fegley, Jr, B. (2015) Lunar volatile depletion due to incomplete accretion within an impact-generated disk. *Nat. Geosci.* **8**, 1–6.

Cartier C., Hammouda T., Boyet M. and Bouhifd M. A. (2014) Redox control of the fractionation of niobium and tantalum during planetary accretion and core formation. *Nat. Geosci.* **7**, 573–576.

Cartier C., Hammouda T., Boyet M., Mathon O., Testemale D. and Moine B. N. (2015) Evidence for Nb 2+ and Ta 3+ in silicate melts under highly reducing conditions: a XANES study. *Am. Mineral.* **100**, 2152–2158.

Corgne A., Liebske C., Wood B. J., Rubie D. C. and Frost D. J. (2005) Silicate perovskite-melt partitioning of trace elements and geochemical signature of a deep perovskitic reservoir. *Geochim. Cosmochim. Acta* **69**, 485–496.

de Koker N., Steinle-Neumann G. and Vlcek V. (2012) Electrical resistivity and thermal conductivity of liquid Fe alloys at high P and T, and heat flux in Earth's core. *Proc. Natl. Acad. Sci. USA* **109**, 4070–4073.

Fiquet G., Auzende A. L., Siebert J., Corgne A., Bureau H., Ozawa H. and Garbarino G. (2010) Melting of Peridotite to 140 Gigapascals. *Science (80-.)* **329**, 1516–1518.

Fischer R. A., Nakajima Y., Campbell A. J., Frost D. J., Harries D., Langenhorst F., Miyajima N., Pollok K. and Rubie D. C. (2015) High pressure metal–silicate partitioning of Ni Co, V, Cr, Si, and O. *Geochim. Cosmochim. Acta* **167**, 177–194.

Frost D. J., Asahara Y., Rubie D. C., Miyajima N., Dubrovinsky L. S., Holzapfel C., Ohtani E., Miyahara M. and Sakai T. (2010) Partitioning of oxygen between the Earth's mantle and core. *J. Geophys. Res. Solid Earth* **115**, 1–14.

Ganguly J. (2009) *Thermodynamics in Earth and Planetary Sciences*.

Gomi H., Ohta K., Hirose K., Labrosse S., Caracas R., Verstraete M. J. and Hernlund J. W. (2013) The high conductivity of iron and thermal evolution of the Earth's core. *Phys. Earth Planet. Inter.* **224**, 88–103.

Kawanishi S., Yoshikawa T. and Tanaka T. (2009) Equilibrium phase relationship between SiC and a liquid phase in the Fe–Si–C system at 1523–1723 K. *Mater. Trans.* **50**, 806–813.

Konôpková Z., McWilliams R. S., Gómez-Pérez N. and Goncharov A. F. (2016) Direct measurement of thermal conductivity in solid iron at planetary core conditions. *Nature* **534**, 99–101.

Labrosse S., Poirier J. P. and Le Mouël J. L. (2001) The age of the inner core. *Earth Planet. Sci. Lett.* **190**, 111–123.

Lay T., Hernlund J. and Buffett B. (2008) Core–mantle boundary heat flow. *Nat. Geosci.* **1**, 25–32.

Li J. and Agee C. B. (2001) The effect of pressure, temperature, oxygen fugacity and composition on partitioning of nickel and cobalt between liquid Fe–Ni–S alloy and liquid silicate: implications for the Earth's core formation. *Geochim. Cosmochim. Acta* **65**, 1821–1832.

Li Y., Dasgupta R. and Tsuno K. (2015) The effects of sulfur, silicon, water, and oxygen fugacity on carbon solubility and partitioning in Fe-rich alloy and silicate melt systems at 3 GPa and 1600 °C: implications for core-mantle differentiation and degassing of magma oceans and reduced plane. *Earth Planet. Sci. Lett.* **415**, 54–66.

MacDonald M. R., Fieser M. E., Bates J. E., Ziller J. W., Furche F. and Evans W. J. (2013) Identification of the +2 oxidation state for uranium in a crystalline molecular complex, [K(2.2.2-Cryptand)][(C 5 H 4 SiMe 3) 3 U]. *J. Am. Chem. Soc.* **135**, 13310–13313.

Malavergne V., Tarrida M., Combes R., Bureau H., Jones J. and Schwandt C. (2007) New high-pressure and high-temperature metal/silicate partitioning of U and Pb: implications for the cores of the Earth and Mars. *Geochim. Cosmochim. Acta* **71**, 2637–2655.

McDonough W. F. (2003) Compositional Model for the Earth's Core. In *Treatise on Geochemistry* (eds. H. D. Holland and K. K. Turekian). Elsevier Ltd., pp. 547–568.

McDonough W. F. and Sun S. (1995) The composition of the Earth. *Chem. Geol.* **120**, 223–253.

Miettinen J. (1998) Reassessed thermodynamic solution phase data for ternary Fe–Si–C system. *Calphad* **22**, 231–256.

Nimmo F. (2015) *Energetics of the Core*. Elsevier B.V.

O'Neill H. S. C. and Eggins S. M. (2002) The effect of melt composition on trace element partitioning: an experimental investigation of the activity coefficients of FeO, NiO, CoO, MoO2 and MoO3 in silicate melts. *Chem. Geol.* **186**, 151–181.

O'Rourke J. G. and Stevenson D. J. (2016) Powering Earth's dynamo with magnesium precipitation from the core. *Nature* **529**, 387–389.

Ohta K., Kuwayama Y., Hirose K., Shimizu K. and Ohishi Y. (2016) Experimental determination of the electrical resistivity of iron at Earth's core conditions. *Nature* **534**, 95–98.

Pozzo M., Davies C., Gubbins D. and Alfè D. (2012) Thermal and electrical conductivity of iron at Earth's core conditions. *Nature* **485**, 355–358.

Pozzo M., Davies C., Gubbins D. and Alfè D. (2014) Thermal and electrical conductivity of solid iron and iron–silicon mixtures at Earth's core conditions. *Earth Planet. Sci. Lett.* **393**, 159–164.

Righter K. (2003) Metal–silicate partitioning of siderophile elements and core formation in the early Earth. *Annu. Rev. Earth Planet. Sci.* **31**, 135–174.

Righter K., Danielson L. R., Pando K. M., Shofner G. A., Sutton S. R., Newville M. and Lee C.-T. (2016) Valence and metal/silicate partitioning of Mo: implications for conditions of Earth accretion and core formation. *Earth Planet. Sci. Lett.* **437**, 89–100.

Sanloup C. and Fei Y. (2004) Closure of the Fe–S–Si liquid miscibility gap at high pressure. *Phys. Earth Planet. Inter.* **147**, 57–65.

Seagle C. T., Cottrell E., Fei Y., Hummer D. R. and Prakapenka V. B. (2013) Electrical and thermal transport properties of iron and iron-silicon alloy at high pressure. *Geophys. Res. Lett.* **40**, 5377–5381.

Siebert J., Badro J., Antonangeli D. and Ryerson F. J. (2012) Metal–silicate partitioning of Ni and Co in a deep magma ocean. *Earth Planet. Sci. Lett.* **321–322**, 189–197.

Turcotte D. L. and Schubert G. (2002) *Geodynamics*, second ed. Cambridge University Press.

Verhoogen J. (1980) *Energetics of the Earth*. National Academy Press, Washington, D.C..

Wade J. and Wood B. J. (2005) Core formation and the oxidation state of the Earth. *Earth Planet. Sci. Lett.* **236**, 78–95.

Wade J. and Wood B. J. (2012) Metal–silicate partitioning experiments in the diamond anvil cell: a comment on potential analytical errors. *Phys. Earth Planet. Inter.* **192–193**, 54–58.

Wohlers A. and Wood B. J. (2015) A Mercury-like component of early Earth yields uranium in the core and high mantle (142) Nd. *Nature* **520**, 337–340.

*Associate editor:* Munir Humayun